Mon. Not. R. Astron. Soc. **000**, 000–000 (0000) Printed 2 February 2008 (MN LaTeX style file v2.2)

arXiv:astro-ph/0404606v2 3 May 2004

The SEDs of the revised 200 mJy sample.

S. Antón^{1,2} $\star$, I.W.A. Browne^{1}, M .J. M. Marchã^{2}, M. Bondi^{3}, A. Polatidis^{4}

^{1} *Jodrell Bank Observatory, University of Manchester, U.K.*
^{2} *CAAUL, Observatório Astronómico de Lisboa, Tapada de Ajuda, 1349-018, Lisboa, Portugal.*
^{3} *Istituto di Radioastronomia del CNR via Gobetti 101, I-40129, Bologna, Italy*
^{4} *Max Planck Institut fur Radioastronomie, Auf dem Hugel 69, Bonn, Germany*

ABSTRACT
We address the question of why low-luminosity radio sources with similar flat radio spectra show a range of optical activity. The investigation is based on the spectral energy distributions (SEDs) of objects from the 200 mJy sample. We gathered new data from the VLA at 43 GHz, from SCUBA in the JCMT at 2000, 1350 and 850 μm and from the ISOPHOT instrument on *ISO* at 170, 90, 60 and 25 μm. There is considerable diversity amongst the SEDs of the objects: there are objects with steep broadband spectra between centimetre and millimetre bands (14% of the sample), there are those with flat broadband spectra over most of the spectral range (48% of the sample) and there are those which show pronounced sub-mm/infrared excesses (27% of the sample). Some objects of the first group have two sided radio morphology indicating that their pc-scale emission is not dominated by beamed jet emission. Amongst the objects that have smooth broadband spectra from the radio to the infrared there are passive elliptical galaxies as well as the expected BL Lacs objects. The most pronounced sub-mm/infrared excesses are shown by the broad emission line objects.

Key words: galaxies: active - galaxies: galaxies: jets - galaxies: photometry - infrared: galaxies - radio continuum.

1 INTRODUCTION

Active galaxies are distinguished by the broad range of the electromagnetic spectrum over which they radiate and by the fact that most of the luminosity comes from the compact nuclear region of the galaxy. Considering the emission in the radio domain, AGNs come, broadly, in two flavours: those with weak radio emission, the "radio-quiet", and those with strong radio emission, the "radio-loud". The radio-loud objects are generally divided further into core-dominated objects and lobe-dominated objects. The former generally have flat radio spectra and it is upon this sub-set of objects we concentrate in this paper. At optical wavelengths, amongst the high-luminosity flat-spectrum AGN, we find objects with strong optical emission lines, the quasars. At lower luminosities we find objects with very weak or absent emission lines and polarised and variable continuum, the BL Lacs, Seyfert-like objects with strong emission lines, and objects with no sign of optical activity, the passive elliptical galaxies. Our primary objective is to investigate the origin of the panoply of optical properties displayed by objects with very similar radio properties, in particular the flat-spectrum, core-dominated, low-luminosity radio sources. The investigation is based on the 200 mJy sample (Marchã 1994, Marchã et al. 1996, hereinafter M96). The sample has been slightly revised as a result of better available data (Antón 2000) and the revised sample is presented here. All the sources are core-dominated when observed with the VLA with 0.2 arcsec resolution at 8.4 GHz and have flat radio spectra between 1.4 and 5 GHz. Their "radio homogeneity", however, disappears at the optical wavelengths: about 30% of the objects show optical properties of BL Lacs, but in the remaining $\sim$ 70% of the objects the optical properties split into broad and narrow emission line objects and apparently inactive elliptical galaxies (M96). The range of optical activity amongst the 200 mJy objects begs the question: why in some objects does the non-thermal component, clearly present in the radio, disappear at optical frequencies? The origin of the split in the optical properties must either arise from differences in the AGN emission and/or differences in the host galaxy properties. In order to try to identify that origin we have embarked in a multi-wavelength study of the 200 mJy sample. This work includes the study of the large-scale properties such as the structure of the host galaxies and the small scale properties, in particular the analysis of the spectral energy distributions of the AGNs. In Marchã et al. (in prep) we present the surface photometry of approximately half of the sample, and we find that the large-scale properties of

---

$\star$ e-mail:Sonia.Anton@oal.ul.pt

the sources are very homogeneous and also similar to those found in radio galaxies in general. In this paper we present the SEDs of the 200 mJy sample, and we pose the following questions:

- Is the lack of optical activity in some objects due to extinction?
- Do all low luminosity flat spectrum radio sources have beamed BL Lac emission?

Extinction could hide core optical non-thermal emission. Radio core-dominated objects are expected to be viewed down the radio axis and thus, according to unification models, should be least likely to be affected by extinction. These models, however, only take into account central obscuring regions, but more extended dusty regions may also be present and prevent us from detecting the AGN emission. The far-infrared band offers the best chance to trace dust emission, and for this reason new infrared data were gathered with the *Infrared Space Observatory* (*ISO*).

In what concerns the second question, the fact that an object has a flat radio-spectrum does not necessarily prove that the emission originates in relativistic jets and is beamed. If the emission comes from self-absorbed lobes, as for example in Compact Symmetric Objects (CSOs), then the flat radio spectrum synchrotron emission is not expected to extend to higher frequency bands. To investigate this, new sub-mm data were gathered with SCUBA. The main astronomical objective of these observations is to try and look how far the synchrotron component extends into the mm/sub-millimetre part of the spectrum. We use VLBI observations (Bondi et al, in prep.) to distinguish between beamed core-jet sources from intrinsically compact and young CSOs.

The framework in which we will discuss the SEDs of the objects is the following:

1. The centimetre wavelength properties of the 200 mJy objects (flat radio spectra plus compact radio structure) are similar to other objects that have dominant synchrotron cores at centimetre wavelengths. Thus we assume that their core radio emission is synchrotron in origin.
2. This synchrotron emission may extend into the sub-mm, infrared and even the optical part of the spectrum. In this latter case one would call the object a BL Lac.
3. Cold dust may contribute to the sub-mm emission.
4. If the optical synchrotron photons are not detected because they are absorbed by dust, an excess of infrared emission (due to reprocessed energy) showing above the extrapolation of the non-thermal broadband spectra might be present.

This paper is organised as follows. In Section 2 the properties of the 200 mJy sample are summarised, the new observations and data reduction are presented. In Section 3 the shape of the SEDs are discussed. The important points of this work are summarised in Section 4. Throughout the paper we assume H_o=50 kms^{-1}Mpc^{-1} and q_o=0.

2 THE SAMPLE, THE OBSERVATIONS AND THE DATA REDUCTION

Table 1. 200 mJy selection criteria

S_{5GHz}	$\alpha_{1.4-5GHz}$	R	δ_{1950}	$\lvert b \rvert$
$\geqslant$ 200 mJy	$\geqslant -0.5$	$\leqslant$ 17 mag	$\geqslant 20^o$	$\geqslant 12^o$

The spectral index α ($S \propto \nu^{\alpha}$) is defined between 1.4 GHz (NVSS catalogue) and 5 GHz (GB6 catalogue), R magnitudes are from APM, corrected by the calibration presented in Antón (2000).

The 200 mJy sample is a radio-selected sample, which comprises all the JVAS (Patnaik et al., 1992; Browne et al., 1998; Wilkinson et al., 1998) sources with core-dominated morphology when observed with the VLA at 8.4 GHz in A-configuration and which obey the criteria presented in Table 1. When the sample was first selected (Marchã 1994), the R magnitudes had been estimated through ocular examination of the Palomar Observatory Sky Survey (POSS) Red plates. This method is fairly good for the bright objects, but some fuzzy objects could have been missed, due to an underestimate of their magnitude. Meanwhile the POSS plates have been digitised by the Automatic Plate Measuring (APM) machine, permitting one to obtain better R magnitudes. This motivated us to re-select the 200 mJy sample, following the criteria in Marchã (1994), but this time the list of objects was constrained by their APM magnitudes. In the process we developed a calibration algorithm that improves the APM magnitudes for blended or fuzzy appearance objects (Antón, 2000). These improved magnitudes were used in the re-selection of the 200 mJy sample.

With the re-selection of the 200 mJy sample, and in comparison with the list of objects presented in M96, seven new objects entered the sample, and one object was subtracted. The later is the object 2214+201. We gathered a spectrum of the object, and the spectrum is identical to that of a M star (Antón, 2000). We also obtained an I image with the Nordic Optical Telescope. Its radial profile is that of a point source and no residuals were found after a PSF subtraction (for details see Antón 2000). We conclude that the detected optical object is most probably a star in front of the radio source. In this case we do not know the R magnitude of the optical counterpart of the radio object, and for this reason the object has been subtracted from the sample. The 200 mJy sample comprises 64 objects, which are listed in Table 2.

M96 obtained optical spectra and optical polarisation for a large number of 200 mJy objects. Based on the equivalent width (EW) of the strongest emission line and the 4000Å break contrast (C; see section 2.1.4) the objects may be classified in four broad categories:

- **BL Lac objects (BLL)**. These are objects with featureless spectra that obey the “classical” BL Lac definition: C $\leqslant$ 0.25 and EW $\leqslant$ 5 Å.
- **BL Lac Candidates (BLC)** These are objects with break contrast 0.25 <C < 0.4 and EW < 40Å.
- **Seyfert-like objects** These are the objects with EW > 60 Å. In this case the value of the 4000Å break does not give a good estimate of the non-thermal continuum, as in most cases there will be contamination from the accretion disk emission, in particular in the case of broad emission line objects. The objects are divided into Seyfert1-like **(Sy1)**, and into Seyfert2-like **(Sy2)** depending whether their emission lines are broad or narrow, respectively.
- **Passive Elliptical Galaxies (PEGs)** These are objects with C $\geqslant$ 0.40 and weak emission lines EW < 30-40 Å.

Table 2. The table contains the following information: 1st column 1959.0 IAU name, 2nd and third columns J2000.0 right ascension and declination respectively, 4th column R magnitudes from APM corrected by the calibration presented in Antón (2000), 5th column redshift, 6th column optical-type classification, 7th column radio morphology as shown by VLBI resolution, 8th column the shape of the broadband SED

Name B1950	*ra* J2000.0	δ J2000.0	R mag	z	Optical type	VLBI type	SED type
0035+227	00 38 08.10	+23 03 28.44	15.6	0.096	PEG	2-S[2]	II
0046+316	00 48 47.14	+31 57 25.09	13.0	0.015	Sy2	c+j[17]	II
0055+300	00 57 48.89	+30 21 08.84	12.5	0.015	PEG	c+j[20]	II
0109+224	01 12 05.82	+22 44 38.80	16.1		BLL	c+j[18]	III
0116+319	01 19 35.00	+32 10 50.01	11.3	0.060	PEG	2-S[3]	II
0125+487	01 28 08.06	+49 01 05.98	16.5	0.067	Sy1	c+j[1]	III
0149+710	01 53 25.85	+71 15 06.47	15.0	0.022	PEG	c+j[1]	II
0210+515	02 14 17.93	+51 44 51.97	16.0	0.049	BLL	c+j[1]	III
0251+393	02 54 42.63	+39 31 34.71	16.0	0.289	Sy1	c+j[8]	III
0309+411	03 13 01.96	+41 20 01.19	17.0	0.134	Sy1	c+j[8]	III
0316+41	03 19 48.16	+41 30 42.10	12.7	0.017	Sy1	2-S[21]	II
0321+340	03 24 41.16	+34 10 45.80	15.5	0.061	Sy1	c+j[10]	III
0651+410	06 55 10.02	+41 00 10.15	13.8	0.021	PEG	c+j[2]	II
0651+428	06 54 43.53	+42 47 58.73	15.0	0.126	BLC	c+j[1]	III
0652+426	06 56 10.55	+42 37 01.34	14.3	0.059	PEG		I
0716+714	07 21 53.45	+71 20 36.36	16.0		BLL	c+j[4]	III
0719+255	07 22 49.04	+25 28 33.92	14.4		UNK		I
0729+562	07 33 28.61	+56 05 41.73	16.7	0.104	PEG		I
0733+597	07 37 30.09	+59 41 03.19	13.7	0.041	PEG	? [16]	I
0806+350	08 09 38.89	+34 55 37.26	15.5	0.082	BLL	c+j[2]	III
0836+290	08 39 15.85	+28 50 39.34	14.9	0.079	PEG	c+j[19]	?
0848+686	08 53 18.90	+68 28 19.01	14.0	0.039	PEG	c+j[2]	I
0902+468	09 06 15.54	+46 36 19.02	16.7	0.084	PEG	2-S[2]	I
0912+297	09 15 52.40	+29 33 23.98	16.6		BLL	c+j[18]	III
0925+504	09 29 15.36	+50 13 34.39	16.7		BLL	c+j[8]	?
1027+749	10 31 22.02	+74 41 58.33	15.5	0.123	Sy1	c+j[10]	?
1055+567	10 58 37.73	+56 28 11.18	16.1	0.144	BLL	c+j[1]	III
1101+384	11 04 27.31	+38 12 31.79	12.6	0.031	BLL	c+j[12]	III
1123+203	11 25 58.74	+20 05 54.38	16.7	0.133	BLL	c+j[10]	III
1133+704	11 36 26.41	+70 09 27.30	13.9	0.046	BLL	c+j[9]	III
1144+352	11 47 22.13	+35 01 07.53	15.0	0.063	PEG	c+j[8]	II
1146+596	11 48 50.36	+59 24 56.36	12.0	0.009	PEG	2-S[15]	II
1147+245	11 50 19.21	+24 17 53.85	17.0		BLL	c+j[5]	III
1215+303	12 17 52.08	+30 07 00.62	15.9	0.130	BLL	c+j[1]	III
1217+295	12 20 06.82	+29 16 50.72	13.7	0.002	Sy1	2-S[2]	II
1219+285	12 21 31.69	+28 13 58.50	15.8	0.102	BLL	c+j[6]	III
1241+735	12 43 11.22	+73 15 59.26	14.2	0.075	PEG	c+j[1]	III
1245+676	12 47 33.33	+67 23 16.46	16.6	0.103	PEG	2-S[2]	I
1246+586	12 48 18.84	+58 20 27.94	15.8		BLL	c+j[16]	III
1254+571	12 56 14.23	+56 52 25.24	12.8	0.041	Sy1	c+j+d[14]	II
1404+286	14 07 00.39	+28 27 14.69	14.7	0.075	Sy1	2-S[13]	II
1418+546	14 19 46.60	+54 23 14.79	15.5	0.151	BLL	c+j[5]	III
1421+511	14 23 14.19	+50 55 37.2	16.6	0.274	Sy1	u [10]	III
1424+240	14 27 00.39	+23 48 00.04	16.5		BLL	c+j[10]	III
1429+400	14 31 20.54	+39 52 40.78	16.7	1.213	Sy1	c+j[10]	?
1532+236	15 34 57.22	+23 30 11.61	11.7	0.018	Sy2	SNR	II
1551+239	15 53 43.59	+23 48 25.48	14.8	0.115	PEG		III
1558+595	15 59 01.70	+59 24 21.85	12.9	0.057	PEG	2-S[1]	II
1645+292	16 47 26.88	+29 09 49.60	16.2	0.132	BLC		I
1646+499	16 47 34.91	+49 50 00.58	16.5	0.045	Sy1	c+j[1]	III
1652+398	16 53 52.22	+39 45 36.61	11.5	0.03	BLL	c+j[11]	III
1658+302	17 00 45.23	+30 08 12.90	12.8	0.036	PEG		III
1703+223	17 05 29.33	+22 16 07.59	12.3	0.049	PEG	c+j[2]	I
1744+260	17 46 48.28	+26 03 20.35	17.0	0.147	Sy2	(c+j[22])	III

Table 2 continued

Name B1950	*ra* J2000.0	δ J2000.0	R mag	z	Optical type	VLBI type	SED type
1755+626	17 55 48.44	+62 36 44.12	11.0	0.024	PEG	? [2]	II
1807+698	18 06 50.68	+69 49 28.11	15.1	0.046	BLL	c+j[7]	III
1959+650	19 59 59.85	+65 08 54.67	16.5	0.047	BLL	c+j[1]	III
2116+81	21 14 01.18	+82 04 48.35	15.5	0.084	Sy1	c+j[15]	III
2202+363	22 04 21.10	+36 32 37.09	16.0	0.073	PEG	u [1]	?
2217+259	22 19 49.74	+26 13 27.96	13.1	0.085	Sy1		II
2227+306	22 29 34.11	+30 57 10.29	16.8	0.322	Sy1		?
2319+317	23 21 54.95	+32 04 07.59	16.0	0.001	UNK		?
2320+203	23 23 20.34	+20 35 23.52	12.8	0.038	PEG	c+j[2]	III
2337+268	23 40 00.84	+27 08 01.37	13.9	0.032	UNK	c+j[2]	II

Keys: 1. Optical classification: **BLL**=BL Lacs, **BLC**=BL Lac Candidates, **Syf1**=Seyfert-1 type, **Syf2**=Seyfert-2 type, **PEG**=Passive Elliptical Galaxies; UNK = Unknown spectrum. 2. Radio morphology classification: **c+j**=core-jet; **c**=core, **c+j+d** Core+jet+disk,**2-S** 2-sided, **u** unresolved. SED classification: **I** steep single power-law broadband spectra, **II** broadband spectra with one or more bumps, **III** broken power-law broadband spectra.

References 1. Bondi et al. (2001) 2. Bondi et al (in preparation) 3. Conway (1996) 4. Gabuzda et al. (1998) 5. Gabuzda et al. (1996a) 6. Gabuzda et al (1996b) 7. Gabuzda et al. (1989) 8. Henstock et al. (1995) 9. Kollgaard et al. (1996) 10. NRAO VLBA calibrators list 11. Pearson et al. (1993) 12. Piner et al. (1999) 13. Stanghellini et al. (2001) 14. Taylor et al. (1999) 15. Taylor et al. (1996) 16. Taylor et al (1994) 17. Ulvestad et al (1999) 18. USNO Astrometric VLBI database 19. Venturi et al (1995) 20. Venturi et al.(1993) 21. Vermeulen et al. (1994) 22. This object shows core-jet morphology at MERLIN resolution (Augusto et al., 1998).

2.1 New data and data reduction

2.1.1 VLA observations – 43 GHz data

As part of a program to measure flux densities of potential high-frequency calibration sources, 16 objects of the 200 mJy sample were observed with the VLA in its D-configuration at 43 GHz. Each observation lasted ∼1 min. The calibration and data reduction were performed in AIPS in the standard manner with 3C286 being used as the primary flux density calibrator.

2.1.2 SCUBA data

We gathered 850, 1350, 2000 μm observations at JCMT[1] using SCUBA[2]. A set of 22 objects was observed between May and July of 1998. The observations were carried by a service observer in a fall-back program, during 32 hours of allocated time. The objects observed were chosen from the 200 mJy list by the observer to fit into the available time and available RA range. Being fall-back observations they were taken during non-optimum weather conditions. The observations were performed in standard SCUBA photometric mode, which involves the conventional technique of chopping and nodding in order to remove the dominant sky background - the chopper throw was 60 arcseconds. The data were processed with SURF (SCUBA User Reduction Facility) package. The reduction process was based on the techniques described in Stevens et al. (1997) and consisted of nod compensation, extinction correction and calibration. The calibrators observed during our observations were: irc+10216, 16293-2422 and Uranus. Starlink package FLUXES supplies the flux densities of the planets for the time and day of observation, corrected for the SCUBA beam-size.

The results of the SCUBA observations are presented in Table 3: flux densities are in mJy and the error on the flux density, eF, includes the calibration uncertainties and the instrumental flux uncertainties, added in quadrature. Table 3 shows that the SCUBA observations were very successful: amongst 22 objects, only one (1558+595) was not detected at any of the 3 SCUBA wavelengths. There are few cases of non-detections at some wavelengths and for these upper limits are quoted as 3σ.

2.1.3 ISOPHOT Observations

A set of seven sources from the 200 mJy sample was observed at 25, 60, 90 and 170 μm wavelengths by *ISO* with the imaging photo-polarimeter ISOPHOT. The list of objects corresponds to the number that could be observed in the total observing time allocated, and obeying : $z \leqslant 0.07$, $|b| > 12^o$, did not belong to GTO programs and their coordinates were permitted by the satellite constraints. The main idea was to compare the SEDs of BL Lac objects with their relatives, and for this aim we selected objects of different optical type: three PEGs, one Seyfert2-like object, two Seyfert1-like object and one BL Lac. The observations were performed with P2 detector to obtain data at 25 μm, C100 detector to obtain data at 60 and 90 μm, and C200 detector to obtain data at 170 μm; all with the same integration time on-source and on-background. Observations at 25 μm were taken with triangular chopper mode with a throw of 60 arcsec between positions. The 60, 90 and 170 μm observations were performed in rectangular chopper mode, the chopper throw was 180 arcsec between positions.

The data were reduced using PIA[3] (PHT-Interactive Analysis). Table 3 presents the results: the flux densities are the mean of the flux densities (obtained from the several chopper

---

[1] James Clerk Maxwell Telescope

[2] Submillimetre Common-User Bolometer Array

[3] PIA is a joint development by the ESA Astrophysics Division and the ISOPHOT consortium.

Table 3. *ISO* and SCUBA data. For each source (IAU name in the first column), the following columns refer to 25, 60, 90 and 170μm *ISO* flux densities and uncertainties (see text), and to the 850, 1350 and 2000 μm SCUBA flux densities and errors (see text).

Name	25μm		60μm		90μm		170μm		850μm		1350μm		2000μm	
	F	σ	F	σ	F	σ	F	σ	F	eF_{850}	F	eF_{1350}	F	eF_{2000}
0046+316	260	57	1139	330	1108	302	1451	300						
0116+319	<9		<372		<165		<264							
0125+487	19	3												
1133+704	<51		<345		66	21	<123		69.9	13.8	56.6	13.1	78.8	13.7
1144+352	11	3	<156		158	40	363	27	86.1	12.7	84.4	12.6	149.2	12.8
1146+596									62.9	13.3	57.6	14.6	94.9	18.3
1147+245									344.9	23.9	337.5	40.5	558.0	32.6
1215+303									153.8	29.6	172.1	21.8	198.8	24.2
1217+295									44.6	11.0	50.4	9.6	37.8	7.3
1219+285									623.9	51.0	635.8	74.0	736.0	41.2
1241+735									39.7	8.9	45.8	9.6	40.6	8.8
1245+676									11.4	3.6	< 13		19.4	2.8
1254+571									78.0	24.5	49.8	12.1	28.1	6.7
1404+286									18.5	5.2	< 16		41.1	9.9
1418+546									170.9	15.6	234.2	28.2	338.5	16.6
1421+511									24.6	4.4	48.3	10.1	69.9	7.7
1424+240									47.1	8.1	151.7	17.9	140.1	10.8
1532+236									455.7	46.9	271.0	32.3	88.1	8.8
1551+239									36.5	4.6	89.8	12.8	125.0	7.4
1558+595	<24		<111		<219		306	86	< 28		< 19		< 30	
1645+292									20.1	6.0	24.6	5.3	26.4	7.5
1646+499	11	3	<126		<108		221	21			205.5	24.9	274.4	13.1
1652+398											452.3	52.9	678.0	26.6
1658+302									30.8	4.3	35.7	6.1	38.1	6.9
1703+223									15.2	3.5				

measurements), and σ is the dispersion of the flux densities about the mean[4]. The systematic error associated with the photometric calibration is estimated to be $\approx$ 30%. The error estimate includes drift and chopper frequency errors (the main sources of uncertainty), and the power calibration error, that contributing $\approx$ 10% of the total error. Considering that there were some problems affecting the ISOPHOT detection system, the most relevant point is the detection of the source. The dispersion of the flux densities (presented in Table 3) is a measure of the statistical significance of the detection. A detection means that the mean flux density is higher than 3σ, otherwise the measurement is considered as a non-detection and an upper limit of 3σ for the flux density is recorded. At 25 μm four out of the seven objects were detected, at 60 μm only one source out of six was detected[5], at 90 μm three out of six were detected and at 170 μm four out of six. Most of the detections look "physically reasonable" and when *IRAS* observations are available for comparison, the *ISO* and *IRAS* detections are consistent.

2.1.4 Optical data

One of the main goals is to compare the properties of the 200 mJy objects at different bands, hence the effort to produce their SEDs. At optical wavelengths much of the light of the low redshift 200 mJy objects is from the host galaxy, however, we are primarily interested in studying the AGN properties, which means that we have to estimate the strength of the extra emission contribution to the optical flux. In order to do this we make use of a common feature of the spectra of early-type galaxies usually referred to as the 4000Å break. This feature which refers to a flux discontinuity occurring across 4000Å is commonly quantified by the break contrast (C) defined as:

$$C = \frac{F_\nu^+ - F_\nu^-}{F_\nu^+} \qquad (1)$$

where F_ν^+ and F_ν^- are the red-ward and blue-ward flux densities of the break, and they are the the mean flux density in the 4050–4250 Å range and 3750–3950 Å range, respectively. If it happens that besides the thermal emission there is an extra source of continuum, then that depression will be decreased, and the measure of contrast as defined in Eq. 1 can then be used to estimate that extra contribution. In a study carried out by Dressler & Shectman (1987) on a large sample of early-type galaxies, the authors concluded that the galaxies showed a very narrow range of contrasts ($< C^G > = 0.49\pm0.1$), with most of them with contrast above 0.4. This led M96 to suggest that optically dull galaxies with measured $C < 0.4$ corresponded to sources where there was an extra contribution due to the AGN (F^{AGN}).

---

[4] The values of σ are the dispersion of the flux densities about the mean; they are not the dispersion on the mean $\sigma/\sqrt{\rm N}$. In a Gaussian distribution the relevant quantity is $\sigma/\sqrt{\rm N}$, a quantity that contains the number of measurements used. However, in our case the data are not statistically well behaved, and σ gives a conservative estimate of the significance of the measurement

[5] The source 0125+487 was only observed at 25 μm

This quantity can be obtained from the observed spectrum via:

$$F^{AGN} = \frac{< C^G > - C}{< C^G >} F_o \qquad (2)$$

where F_o is total optical flux density. Making use of the spectra in M96 we have obtained an estimate of the contribution of the AGN to the optical flux. The working assumption is that the extra continuum represents the nuclear component. The origin of the nuclear emission might be thermal from accretion disk emission, or non-thermal. The approach here represents an effort to minimise as much as possible the contribution of starlight, which for some objects is clearly the major source of emission in the optical band. For those objects whose contrasts are C> 0.45, C=0.45 was adopted in order to have a quantitative upper limit to the nuclear emission. The flux calibration of the spectra in M96 is reliable at a 10% level (Antón 2000). This level of accuracy is sufficient for the SED analysis.

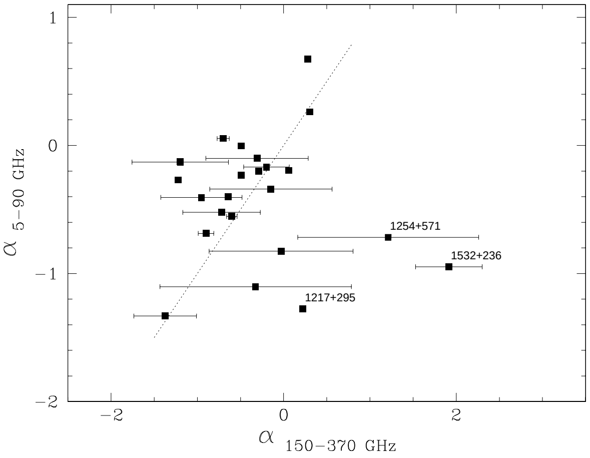

Figure 1. The spectral indices at the sub-mm band vs the spectral indices at the radio band (see text). The dashed line represents $\alpha_{\rm sub-mm} = \alpha_{\rm radio}$.

3 DISCUSSION OF THE SEDS

In Figure A1 we present the SEDs for all the objects in the 200 mJy sample. To supplement our own data we have plotted and used in the following analysis relevant data found in the NASA Extragalactic database (NED) and in the literature. In particular we include measurements from *IRAS*, from *2MASS* and from the *ROSAT* All-Sky-Survey (Voges et al. 1999). We see a considerable diversity both in the spectral coverage and in the overall shapes of the SEDs. If we discount those objects with very poor spectral coverage in the sub-mm and infrared parts of the spectrum, we can tentatively identify three broad spectral types of objects: (a) those with initially steep radio power-law spectra ($\alpha < 0.4$) and perhaps steepening onto the sub-mm/IR/optical bands, (b) the objects that show an infrared bump that we interpret as dust emission and (c) the broken power-law objects that show flat broadband spectra up to the millimetre band, and sometimes beyond, before steepening. We also list these classifications in Table 2, as class I, II and III, respectively. Nearly all the known BL Lac objects fall into the third, broken power-law, category. It is interesting that, with the exception of 1418+546, any flux variability is insufficient to show up in plots of this crude flux resolution. It should also be noted that a few PEGs (e.g. 0055+300) look similar to BL Lacs when we discount the near infrared/optical emission which is predominantly starlight, not AGN emission. There are more PEGs where just the sub-mm emission appears as a smooth continuation of the radio spectrum. We discuss this further below. A typical steep spectrum object is 0035+227 and one with a lumpy spectrum 1404+286. We now look at the different spectral ranges individually.

3.1 From the radio to the submillimetre

One of the main goals is to establish if the synchrotron emission extends up to the sub-mm band. We look to see whether, statistically, the sub-mm emission can be described as a smooth extension of what we already know to be synchrotron emission, i.e. the radio emission, or if there is a discontinuity indicating additional thermal emission from cold dust. From Figure A1 it is noticeable that the majority of the objects show a spectrum consistent with a power-law continuing from the radio to the sub-mm wavelengths, suggesting that the synchrotron emission does indeed extend up to the sub-mm band. Assuming that the emission may be represented by a power-law (F $\sim$ ν^{α}), the spectral indices $\alpha_{\rm radio}$ and $\alpha_{\rm sub-mm}$ were computed through a weighted least-square fit to the (available) data between $5 \leqslant \nu < 90$ GHz and $150 \leqslant \nu \leqslant 370$ GHz respectively. Errors are not quoted for $\alpha_{\rm radio}$ because the data were not gathered simultaneously or with instruments of the same angular resolution; it is very difficult to quantify the effects of variability and resolution. For the same reason, errors of $\alpha_{\rm sub-mm}$ are not quoted if the data were taken in different epochs. In Figure 1 the dashed line represents $\alpha_{\rm sub-mm} = \alpha_{\rm radio}$. The large majority of the 200 mJy objects are grouped on or just to the left of the $\alpha_{\rm sub-mm} = \alpha_{\rm radio}$ line, indicating either the same or a slightly steeper spectral index at sub-mm wavelengths compared to the radio. This is what is expected for synchrotron emission with a power-law energy spectrum modified at the highest energies by synchrotron losses. The objects 1217+295, 1254+571, 1532+236 depart from the general trend and are discussed individually in Section A. Considering the sub-mm properties of the different optical-classes, we find the following[6]:

BL Lac objects – The mean sub-mm spectral index is $\overline{\alpha}_{\rm sub-mm}=-0.25\pm0.37$ which is consistent with -0.48 ± 0.22 obtained by Gear et al (1994) for a sample of 30 BL Lacs. Not surprisingly, all the objects have flat radio spectra and flat sub-mm spectra, in good agreement with previous studies (e.g., Knapp, Bies, & van Gorkom 1990, henceforth K90, Bloom et al. 1994, Gear et al. 1994).

Seyfert1-like objects – In this group we find diverse SEDs, with objects showing a falling spectrum and others showing a rising spectrum. The $\alpha_{\rm sub-mm}$ distribution is broad, the mean sub-mm spectral index is $\overline{\alpha}_{\rm sub-mm} = -0.43 \pm 0.87$.

---

[6] Unfortunately the numbers per class for Seyfert2-like and BLC are so small that they had to be excluded from the above analysis.

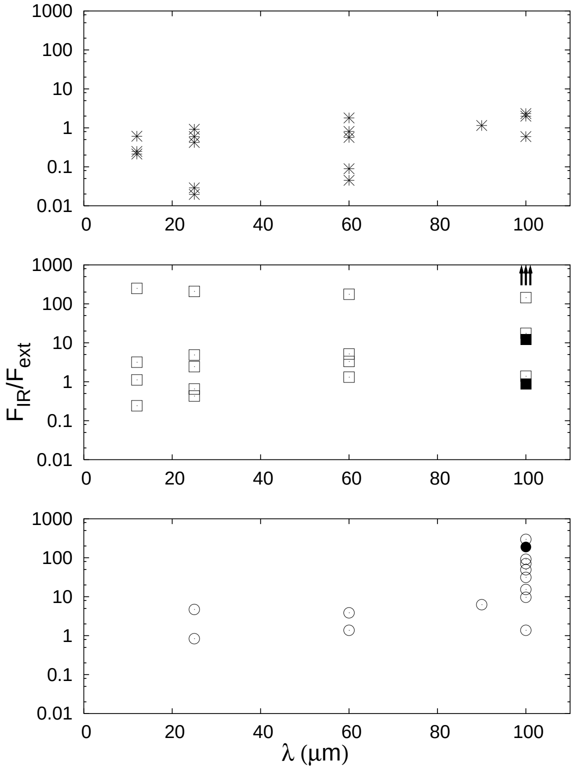

Figure 2. The ratio between the flux density detected at 12, 25, 60, 90 and 100 μm, F_{IR}, and the flux density extrapolated from the radio/sub-mm band , F_{ext}, for different objects. Stars represent BL Lacs (top panel), square symbols represent Seyfert-like objects (middle panel) and circles represent PEGs (lower panel). An object may not have been detected at the all wavelengths. In the case of 3 objects, the data are from 170μm and they are represented by filled symbols at 100μm. The Seyfert-like objects 1217+295, 1254+571 (Mrk 231) and 1532+236 (Arp 220) are the only objects with $F_{IR}/F_{ext}>>1000$, being represented by arrows (see middle plot).

PEG objects – These objects have flattish sub-mm spectra and their mean spectral index is $\overline{\alpha}_{\rm sub-mm} \sim -0.58\pm0.39$.

In summary, we do not find a clear split of properties between the radio and sub-mm band that could account for the split of properties detected in the optical regime. Broadly, the SEDs of the objects up to the submillimetre regime (and for the list of the objects presented in Table 3) are similar.

3.2 The infrared emission

The far- and mid-infrared properties of some of the 200 mJy objects are analysed using our own *ISO* data and archival *IRAS* data. The main goal is a) to investigate if, for a given optical magnitude of the host galaxies, the 200 mJy objects have an excess of infrared emission compared to normal radio-quiet elliptical galaxies and, b) to investigate the nature of the infrared excess; i.e. is it mainly synchrotron emission or is it dust emission?

K90 compared the *IRAS* infrared luminosities of normal E/S0 galaxies with radio galaxies and found that the latter have stronger infrared emission relative to the optical emission than do normal E/S0 galaxies. In order to investigate how much of the infrared emission of the 200 mJy objects can be attributed to the “normal” emission of the host galaxy, we computed the median value of the ratio of the luminosity at 90μm/170μm (*ISO* data) or 100 μm (*IRAS* data) with the luminosity in the B band, L_{IR}/L_B, and compared it with K90 findings for normal galaxies. We chose the far-infrared fluxes because they correspond to the wavelengths where detections are above 50% in both our and K90 case. We found that the median L_{IR}/L_B is 1.93 for the detected 200 mJy objects [7], which is one order of magnitude higher than $L_{IR}/L_B= 0.12$ found by K90 for radio elliptical galaxies. Comparing with $L_{IR}/L_B= 0.041$ for E/SO/SOa galaxies from K90 we find that our objects are almost two orders of magnitude brighter in the infrared than normal galaxies. Thus, even if part of the infrared emission of the 200 mJy objects is due to the host galaxy, there needs to be another infrared component to account for the total infrared emission. We now investigate the origin of the “extra” infrared emission.

Figure 2 shows the ratio between the detected flux densities in the infrared band with estimates of the non-thermal flux densities extrapolated from the radio/sub-mm band, F_{IR}/F_{ext}, at each of the *IRAS* wavelengths and divided into PEGs, Seyfert1-like objects and BL Lac objects. Note that the extrapolated non-thermal emission represents an upper estimate since it assumes that the radio/sub-mm spectrum continues as power-law to higher frequencies. Figure 2 shows that there are objects with F_{IR} similar to F_{ext}, and

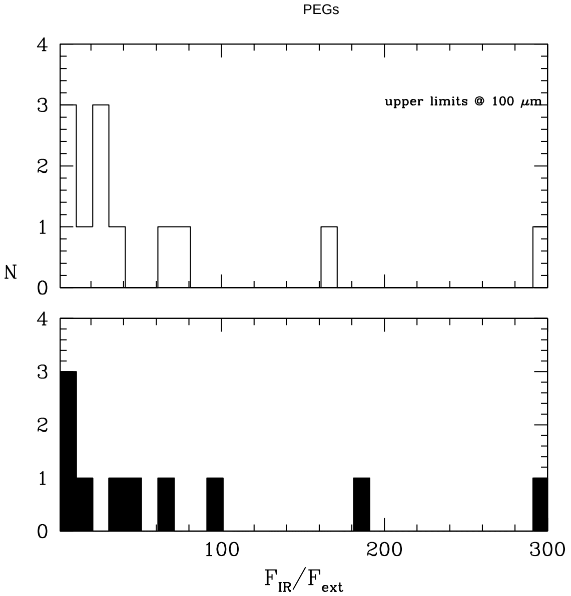

Figure 3. Bottom ratio between the flux density detected at the largest infrared wavelength available (90, or 100, or 170 μm), and the flux density extrapolated from the radio/sub-mm band at that wavelength for the PEGS **Top** ratio between an upper limit of the flux density at 100 μm, and the flux density extrapolated from the radio/sub-mm band at 100μm for the PEGS.

---

[7] The mean value is $<L_{IR}/L_B>= 5.0$ with a r.m.s. = 7.97

this is what one would expect for a smooth synchrotron spectrum, and objects in which the infrared emission is clearly much stronger than the extrapolated non-thermal emission, and the dominant emission process must be thermal, i.e. dust emission[8]. As far as the properties of the objects as a group are concerned, the properties of BL Lacs, Seyfert-like objects and PEGs split in the infrared band:

- The BL Lacs have $F_{IR}/F_{ext} < 2$. They are the only group that as a whole shows smooth broadband spectra from the radio up to the infrared.

- The PEG objects show a range of F_{IR}/F_{ext}, with a fraction showing sub-mm/infrared excesses particularly important at relatively large wavelengths (see Fig. 2), thus suggesting the presence of cold dust. We have infrared data for 12 out of 22 PEGs. In order to investigate whether the remaining fraction of PEGs might have a big far-infrared bump, we obtained from the IRAS Scan Processing and Integration tool upper limits of the flux density at the location of the non-detected PEG. Figure 3 shows the distribution of F_{IR}/F_{ext} [9] of PEGs: in the lower plot F_{IR} represents the detected flux density, whereas in the upper plot F_{IR} represents an upper limit of the flux density at 100 μm. The distributions are similar. With the available information, the only conclusion is that objects with strong infrared bumps as those shown by objects like Arp 220 are unlikely to be frequent amongst the non-detected PEGs.

It is possible to estimate the dust mass of the objects with *ISO* and/or *IRAS* data and for which there is a clear visual evidence in the SEDs for dust emission. For some of the objects dust mass estimates were found in the literature, e.g. we found from K90: $M^{d}_{0055+300} = 8.5\times10^{6} M_{\odot}$ and $M^{d}_{0116+319} = 1.4\times10^{8} M_{\odot}$. For the objects with new data, the radio to infrared broadband spectra were fitted assuming a power-law component plus a greybody component, $F_\nu = F_{pl} + F_{gb}$, $F_{pl} \sim \nu^{\alpha}$ and $F_{gb} \sim \nu\, I(\nu,T)$ (Hildebrand, 1977). Figure 4 shows an example of the fitted model for 1144+352. The dust temperature can be estimated and the mass of the dust responsible for the far-infrared emission was computed according to K90:

$M^{d} = 4.8\, d_L^2\, (e^{\frac{144}{T_d}} - 1)\, F_{100}\, M_{\odot}$, where $d_L = \frac{zc}{H_o}(1 + \frac{z}{2})$ is the luminosity distance (in Mpc) and F_{100} is the thermal emission at 100 μm (in Jy). We obtained:

$(M^{d}/M_{\odot})_{1144+352} = 7\times10^{7}$ $T^{d}=22$
$(M^{d}/M_{\odot})_{1146+596} = 3\times10^{5}$ $T^{d}=36$
$(M^{d}/M_{\odot})_{1558+595} = 1\times10^{8}$ $T^{d}=22$

From IRAS Scan Processing and Integration tool we obtained the flux densities at 100μm for a list of 5 objects. No new data was gathered for these objects, and dust mass estimates are based on published data; they are:

$(M^{d}/M_{\odot})_{0035+227} = 8\times10^{7}$ $T^{d}=37$
$(M^{d}/M_{\odot})_{0149+710} = 9\times10^{6}$ $T^{d}=37$
$(M^{d}/M_{\odot})_{0651+410} = 7\times10^{7}$ $T^{d}=21$
$(M^{d}/M_{\odot})_{1755+626} = 5\times10^{6}$ $T^{d}=29$

These results indicate the existence of cold dusty regions (20<T<50 K) with dust masses similar to those found in typical early-type galaxies, i.e. $M^{d} \sim 10^{5} - 10^{7} M_{\odot}$ (e.g. Wiklind 1995). One way dust might be also detectable is by its effect on the optical emission lines. Serote Roos & Gonçalves (2004) have concluded that this is not the case for these objects. They have examined the spectroscopic properties of 90% of the PEGs of the 200 mJy sample and found that the dust content associated with the emitting regions is small ($E(B-V) < 0.25$). Thus, even if there is good evidence for the presence of dusty regions in PEGs, extinction is not the main cause of the low level of activity in these objects.

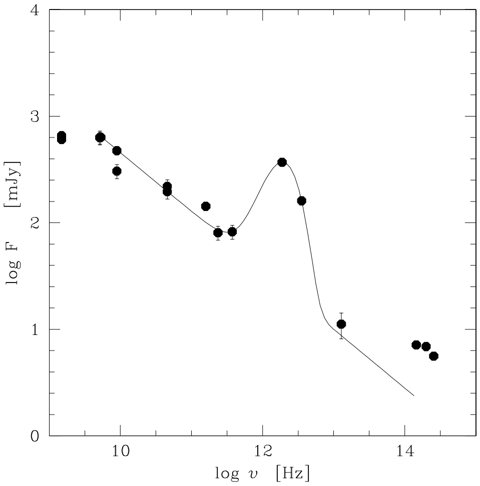

Figure 4. Broadband spectrum of 1144+352, in units of log F_ν vs log ν. Data points include data from the literature and the ISO and SCUBA data presented here. The spectrum was fitted with a power-law component plus a greybody component (see text).

- Seyfert1-like objects tend to have lower sub-mm/infrared excesses than PEGs (see Figure 2), eventhough there are some exceptions, with objects having $F_{IR}/F_{ext} >> 100$. This set comprises 1217+295, 1254+571 (Mrk 231), 1532+236 (Arp 220), all objects that are known to have large quantities of dust (see notes on individual sources in Appendix A). We note that some Seyfert-like objects show F_{IR}/F_{ext} similar to those shown by BL Lac objects. In those cases the emission is probably non-thermal in origin.

3.3 The SEDs and radio morphology

In this section we look for any connection between the shapes of the SEDs and the type of radio-structure of the sources. We have a heterogeneous selection of VLA observations ranging in resolution from 0.2 to 45 arcsec and we have VLBI observations down to a resolution of ~2 mas. All objects were initially selected to have compact cores which are the dominant features in the 0.2 arcsec resolution VLA

---

[8] Not withstanding the previous discussion it has been suggested that non-thermal flares could account for infrared excess in some objects (van Bemmel, Barthel, & de Graauw 2000). But, since flares are a short lived phenomenon, it would be very peculiar if all sources showing infrared excess (over the extrapolated radio emission) were observed at a moment of a flare.

[9] F_{ext} as before and F_{IR} being the flux density at 100 micron, or 90/170 if observed with ISO

8.4 GHz maps. In addition to these 8.4 GHz VLA observations, all objects are in the NVSS Catalogue (Condon et al. 1998), which gives information on any radio structure larger than about an arc-minute. A particularly important question is whether or not the compact radio emission comes from a nuclear jet and this is why we focus in the VLBI data here. There are VLBI observations of 58 of the 64 sources in the sample and in Table 2 we present the current best classification of the structures in terms of one-sided core-jet (C-J), two sided (2-S), unresolved single component (U), or unclassified when the morphology was too complex or ill-defined. In the 2-S category we include all the objects with jet and/or lobe emission on both sides of the core or core candidate. This is a somewhat simplistic classification scheme, but our main intention here is just to separate objects in which the pc-scale emission is clearly dominated by a beamed jet component (C-J) from the others (2-S). The 2-S sources contain also some Compact Symmetric Objects and CSO candidates which are intrinsically small and young objects.

There are 9 objects that are classified as 2-S. Most of them (6) are classified as PEGs, 4 have an infrared bump in the SED suggesting the presence of dust emission, and the remaining 2 have a steep power-law spectrum. In these the dominant radio emission might *not* come from the core but from compact self-absorbed lobes. In that case, we would not expect the synchrotron emission from these lobes to be detectable at millimetre or optical wavelengths. This expectation is supported by the SEDs.

There are 40 objects that are classify as having a core-jet radio structure and it is in this sub-set of objects that we look how far the synchrotron core emission extends up in the electromagnetic spectrum. We would expect many of these to have broken power-law SEDs. Twenty eight of the 40 sources do, while the rest are divided between types I, II and unclassified SEDs. It is of little surprise that 18 of the 28 core-jet radio objects which have broken power-law SEDs, are classified as BL Lacs. In addition, one more is a BL Lac candidate. The remaining nine are broad-line (6) and narrow-line (1) objects and PEGs (2). We find the high proportion of broad-line objects with broken power law a somewhat surprising result since in these objects we might expect the optical and near-infrared emission to be dominated by accretion disk or dust re-processed emission, respectively. Two of the six have already been noted as unusual objects having “hybrid” properties intermediate between BL Lac objects and Seyfert galaxies; they possess both a broad-line region and polarised optical continuum emission (Marchã et al, 1996; Jackson and Marchã, 1999). Perhaps, some of the other four objects might be similar hybrids. We note that none of the PEGS look like infrared/optical synchrotron emitters – they would not be classified as PEGS if they did. However, there are core-jet objects, like 0055+300 and 1144+352, whose radio-to-submm spectra suggest synchrotron emission but whose SEDs in the infrared are distorted by additional dust emission.

4 CONCLUSIONS

The main goal of this work was to investigate the origin of the diverse optical activity amongst similar radio-loud low-luminosity flat-spectrum objects. The investigation was based on the 200 mJy sample, a radio-selected sample showing a range of optical activity. To achieve that goal, multi-wavelength observations were obtained (millimetre data with VLA, sub-mm data with SCUBA and infrared data with *ISO*). Adding data from the literature allowed us to produce the SEDs of 64 objects. The SEDs were analysed with two main goals: to characterize the non-thermal synchrotron component and to search for dust emission. Our findings may be summarised as follows:

(i) There is considerable diversity amongst the SEDs but objects fall broadly into three groups: there are objects with steep spectra between 1.4 GHz and 43 GHz (14% of the sample), there are those with flat spectra over most of the spectral range (48% of the sample) and there are those which show pronounced sub-mm/infrared excesses (27% of the sample).

(ii) Sub-mm observations indicate that a major fraction of the 200 mJy objects have smooth and flattish synchrotron spectra up to the sub-mm band. This includes BL Lacs, BL Lac Candidates, and some Seyfert1-like and PEG objects. In only few cases the dominant sub-mm emission mechanism is clearly thermal dust emission (for example, Arp 220 and Mrk 231).

(iii) The broadband spectra between radio and infrared wavelengths suggest that different objects have different dominant emission mechanisms in the infrared band. Some objects show a smooth broadband spectrum which can be explained by synchrotron emission – all BL Lac and some broad-emission line objects are in this group. Others show moderate infrared excess over the extrapolated radio/submillimetre emission, suggesting that both synchrotron emission and dust emission contribute to the infrared – this group includes broad and narrow emission line objects and PEGs. The far-infrared bump present in the majority of the PEGs indicates the presence of cold dust, which mass we estimate to be similar to that found in typical early-type galaxies. Even though there is dust emission the analysis of Serote Roos & Gonçalves (2004) suggests that it is not strongly affecting the line emission regions. Thus extinction is unlikely to account for the low level of observed activity on PEGs.

(iv) Correlating the broadband SED shapes with the radio morphology (through high resolution radio images available in the literature) allow us to conclude that the sources with two sided morphologies nearly all have falling spectra between 1.4 GHz and 43 GHz. Not surprisingly, all the sources showing core-jet radio morphology have flat broadband spectra often extending well into the sub-mm/infrared range. The vast majority of these are spectroscopically classified as BL Lacs or Seyfert-like objects. In a subsequent paper we will discuss in more detail the SEDs of those objects that are synchrotron emitters, independently of the optical classification. We will compare their spectra with those of blazars, in general, and suggest that there may be many more objects with low frequency peaks in their synchrotron spectra than has been previously thought.

5 ACKNOWLEDGMENTS

We thank our anonymous referee for very constructive comments. SA acknowledges all the support during the visit to the ISOPHOT Data Centre in Heidelberg. SA acknowledges the financial support from the European Commission, TMR Programme, Research Network Contract ERBFMRXCT96-0034 "CERES", and from the Portuguese Fundação para a Ciência e Tecnologia through the grant SFRH/BPD/5692/2001. M.J.M. M. acknowledges the financial support from the Portuguese Fundação para a Ciência e Tecnologia through the grant SFRH/BPD/3610/2000 This research has made use of the NASA/IPAC Extragalactic Database (NED) which is operated by the Jet Propulsion Laboratory, California Institute of Technology, under contract with the National Aeronautics and Space Administration. "This research has made use of the NASA/ IPAC Infrared Science Archive, which is operated by the Jet Propulsion Laboratory, California Institute of Technology, under contract with the National Aeronautics and Space Administration."

REFERENCES

Antón, S., 2000, PhD thesis, University of Manchester.
Augusto, P., Wilkinson, P. N. & Browne, I. W. A., 1998, MNRAS, 299, 1159.
Bloom, S. D., Marscher, A. P., Gear, W. K., Terasranta, H., Valtaoja, E., Aller, H. D. & Aller, M. F., 1994, AJ, 108, 398.
Bondi, M., Marchã, M. J. M., Dallacasa, D., & Stanghellini, C. 2001, MNRAS, 325, 1109.
Browne, I. W. A., Wilkinson, P. N., Patnaik, A. R., & Wrobel, J. M. 1998, MNRAS, 293, 257
Carollo, C. M., Franx, M., Illingworth, G. D., & Forbes, D. A. 1997, ApJ, 481, 710.
Condon, J. J., Cotton, W. D., Greisen, E. W., Yin, Q. F., Perley, R. A., Taylor, G. B., & Broderick, J. J. 1998, AJ, 115, 1693.
Conway, J. E., 1996, IAU Symp. 175: Extragalactic Radio Sources, 92.
de Bruyn, A. G., Wieringa, M., Barthel, P.D., O'Dea, C. P. & Schilizzi, R. T., 1991, NFRA Newsletter, Issue nr 4 - July.
Dressler, A. & Shectman, S. A. 1987, ApJ, 94, 899.
Gabuzda, D. C., Cawthorne, T. V., Roberts, D. H. & Wardle, J. F. C, 1989, ApJ, 347, 701.
Gabuzda, D. C., Sitko, M. L. & Smith, P. S., 1996, AJ, 112, 1877.
Gabuzda, D. C. & Cawthorne, T. V., 1996, MNRAS, 283, 759.
Gabuzda, D. C., Kovalev, Y. Y., Krichbaum, T. P., Alef, W., Kraus, A., Witzel, A. & Quirrenbach, A., 1998, A&A, 333,445.
Gear, W. K., Stevens, J. A., Hughes, D. H., Litchfield, S. J., Robson, E. I., Terasranta, H., Valtaoja, E., Steppe, H., Aller, M. F. & Aller, H. D., 1994, MNRAS, 267, 167.
Henstock, D. R., Browne, I. W. A., Wilkinson, P. N., Taylor, G. B., Vermeulen, R. C., Pearson, T. J. & Readhead, A. C. S., 1995, ApJS, 100, 1.
Hildebrand, R. H. 1983, QJRAS, 24, 267.
Hildebrand, R. H., Whitcomb, S. E., Winston, R., Stiening, R. F., Harper, D. A., & Moseley, S. H. 1977, ApJ, 216, 698.
Jackson, N. & Marchã, M. 1999, MNRAS, 309, 153.
Knapp, G. R., Bies, W. E., & van Gorkom, J. H. 1990, AJ, 99, 476 (K90).
Kollgaard, R. I., Gabuzda, D. C. & Feigelson, E. D., 1996, ApJ, 460, 174.
Marchã, M. J. M., 1994, PhD thesis, University of Manchester
Marchã, M. J. M., Browne, I. W. A., Impey, C. D. & Smith, P. S. 1996, MNRAS, 281, 425 (M96)
Patnaik, A. R., Browne, I. W. A., Wilkinson, P. N., & Wrobel, J. M. 1992, MNRAS, 254, 655
Pearson, T. J., Readhead, A. C. S., Barthel, P. D., Conway, J. E. & Myers, S. T., 1993, AAS, 25, 869.
Piner, B. G., Unwin, S. C. Wehrle, A. E., Edwards, P. G., Fey, A. L. & Kingham, K. A., 1999, ApJ, 525, 176.
Stanghellini, C., Dallacasa, D., O'Dea, C. P., Baum, S. A., Fanti, R. & Fanti, C., 2001, A&A, 377, 377.
Taylor, G. B., Silver, C. S., Ulvestad, J. S. & Carilli, C. L., ApJ, 519, 185.
Taylor, G. B., Vermeulen, R. C., Readhead, A. C. S., Pearson, T. J., Henstock, D. R. & Wilkinson, P. N., 1996, ApJS, 107, 37.
Taylor, G. B., Wrobel, J. M., & Vermeulen, R. C. 1998, ApJ, 498, 619.
Sanders, D. B., Soifer, B. T., Elias, J. H., Madore, B. F., Matthews, K., Neugebauer, G., & Scoville, N. Z. 1988, ApJ, 325, 74
Serote Roos, M. & Gonçalves, A. C. 2004, A&A, 413, 91
Stevens, J. A., Ivison, R. J. & Jenness, T. 1997, SCUBA photometry cookbook
Ulvestad, J. S., Wrobel, J. M., Roy, A. L., Wilson, A. S., Falcke, H. & Krichbaum, T. P., 1999, ApJL, 517, L81.
van Bemmel, I. M., Barthel, P. D., & de Graauw, T. 2000, A&A, 359, 523
Venturi, T., Giovannini, G., Feretti, L., Comoreto, G. & Wehrle, A. E., 1993, ApJ, 408, 81.
Venturi, T., Castaldini, C., Cotton, W. D., Feretti, L., Giovannini, G., Lara, L., Marcaide, J. M. & Wehrle, A. E., 1995, ApJ, 454, 735.
Vermeulen, R. C., Readhead, A. C. S. & Backer, D. C., 1994, ApJL, 430, L41.
Voges, W.,Aschenbach, B., Boller, T., Bräuninger, H., Briel, U., Burkert, W., Dennerl, K., Englhauser, J., Gruber, R., Haberl, F., Hartner, G., Hasinger, G., Kürster, M., Pfeffermann, E., Pietsch, W., Predehl, P., Rosso, C., Schmitt, J. H. M. M., Trümper, J. & Zimmermann, H. U.,1999, A&A, 349, 389.
Wiklind, T., Combes, F., & Henkel, C. 1995, A&A, 297, 643
Wilkinson, P. N., Browne, I. W. A., Patnaik, A. R., Wrobel, J. M., & Sorathia, B. 1998, MNRAS, 300, 790

APPENDIX A: NOTES ON INDIVIDUAL SOURCES

• 1146+596 – Its SED suggests that the non-thermal cut-off might happen in the sub-millimetre regime. This is a core-dominated source at JVAS resolution ($0.2''$), however VLBI monitoring at 5 GHz revealed twin relativistic jets in a scale of miliarcseconds (Taylor, Wrobel, & Vermeulen 1998). We note that the absence of large-scale radio emission in NVSS map might indicate that this is a young radio source.

- 1217+295 (NGC 4278) is a well known radio galaxy. The broadband spectrum between 5 and 43 GHz is relatively steep, and the sub-mm emission is likely to be thermal, something that is consistent with the detection of large-scale dusty regions reported by Carollo et al. (1997).
- 1245+676 – NVSS map reveals a large Mpc FRII morphology, but the VLBA map shows that the core has a symmetric structure with two mini-lobes (de Bruyn et al. 1991). This is a so called 'double-double' source.
- 1254+571 (Mrk 231) and 1532+236 (Arp 220) – They have a strong inverted sub-mm spectra – both objects are Ultra-luminous Infrared galaxies (e.g. Sanders et al. 1988). The $\alpha_{\rm sub-mm}$ of 1532+236 is 1.91± 0.39 and the $\alpha_{\rm sub-mm}$ of 1254+571 is 1.21±1.04.
- 1404+286 – This is a Seyfert1-like object. The broadband spectrum is inverted in the radio and steep between the radio and the sub-mm band, with $\alpha_{\rm radio} \sim \alpha_{\rm sub-mm}$. 1404+286 is one of the best examples of Gigahertz Peak Sources (GPS), the peak occurring at 5 GHz.

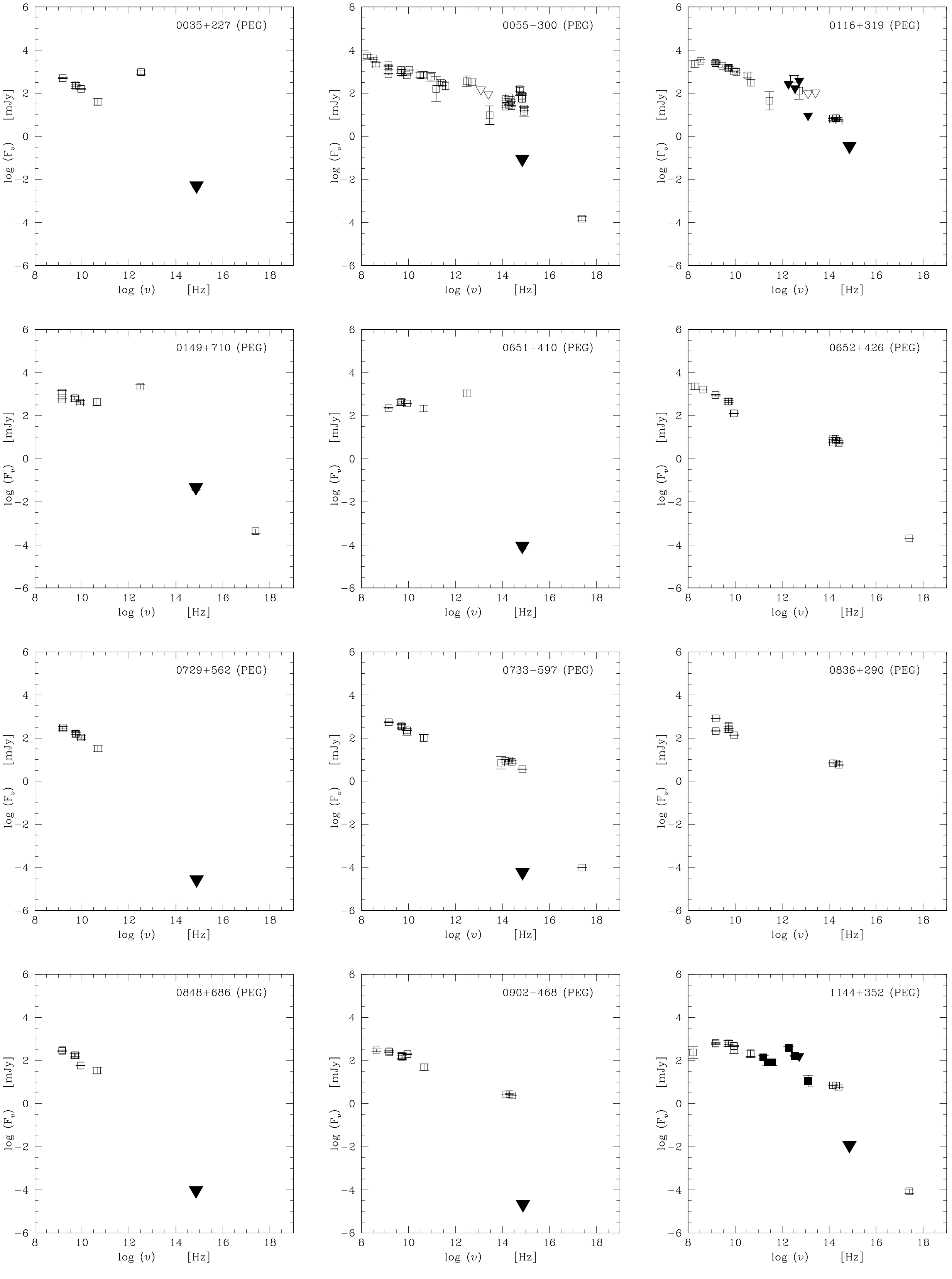
0035+227 (PEG)
0055+300 (PEG)
0116+319 (PEG)
0149+710 (PEG)
0651+410 (PEG)
0652+426 (PEG)
0729+562 (PEG)
0733+597 (PEG)
0836+290 (PEG)
0848+686 (PEG)
0902+468 (PEG)
1144+352 (PEG)
log (F_ν) [mJy]
log (ν) [Hz]
6
4
2
0
−2
−4
−6
8
10
12
14
16
18

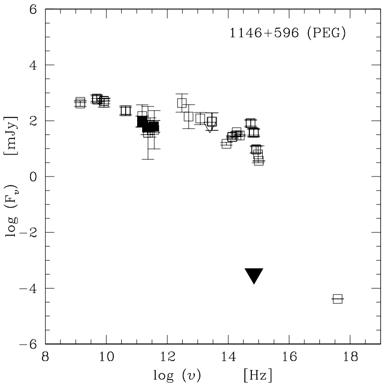
1146+596 (PEG)
log (F_ν) [mJy]
log (ν) [Hz]
6
4
2
0
−2
−4
−6
8
10
12
14
16
18

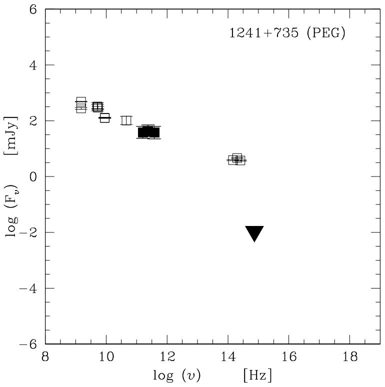
1241+735 (PEG)
log (F_ν) [mJy]
log (ν) [Hz]
6
4
2
0
−2
−4
−6
8
10
12
14
16
18

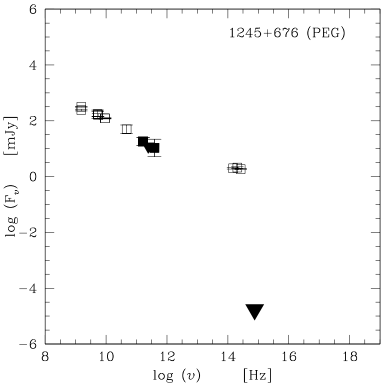
1245+676 (PEG)
log (F_ν) [mJy]
log (ν) [Hz]
6
4
2
0
−2
−4
−6
8
10
12
14
16
18

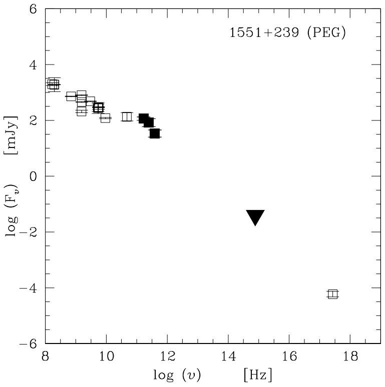
1551+239 (PEG)
log (F_ν) [mJy]
log (ν) [Hz]
6
4
2
0
−2
−4
−6
8
10
12
14
16
18

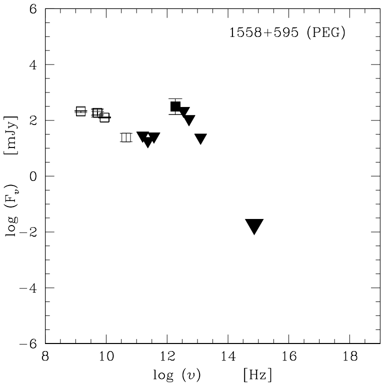
1558+595 (PEG)
log (F_ν) [mJy]
log (ν) [Hz]
6
4
2
0
−2
−4
−6
8
10
12
14
16
18

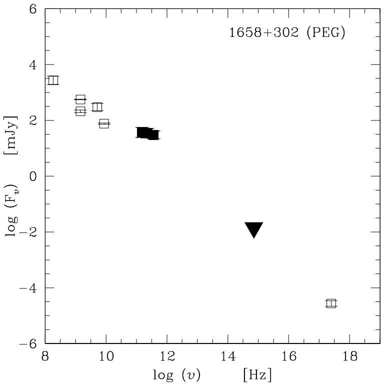
1658+302 (PEG)
log (F_ν) [mJy]
log (ν) [Hz]
6
4
2
0
−2
−4
−6
8
10
12
14
16
18

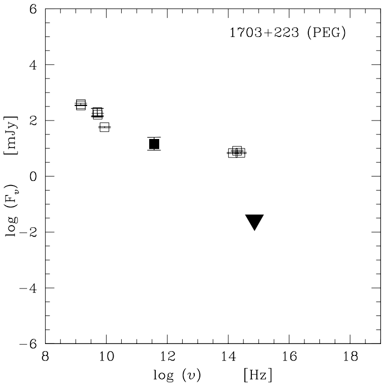
1703+223 (PEG)
log (F_ν) [mJy]
log (ν) [Hz]
6
4
2
0
−2
−4
−6
8
10
12
14
16
18

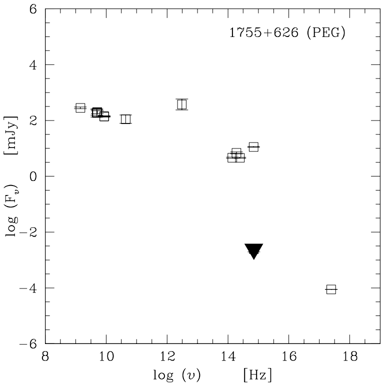
1755+626 (PEG)
log (F_ν) [mJy]
log (ν) [Hz]
6
4
2
0
−2
−4
−6
8
10
12
14
16
18

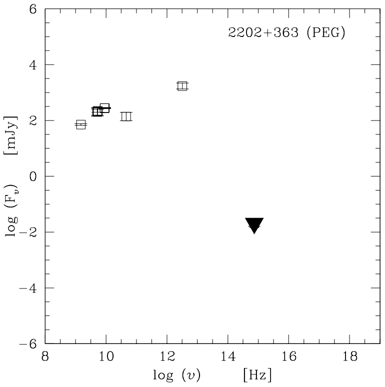
2202+363 (PEG)
log (F_ν) [mJy]
log (ν) [Hz]
6
4
2
0
−2
−4
−6
8
10
12
14
16
18

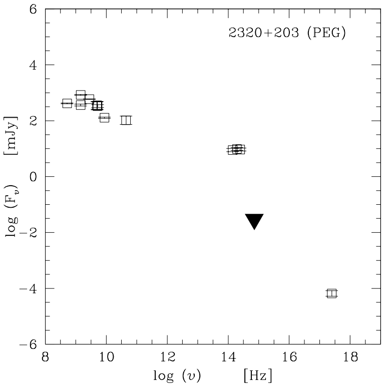
2320+203 (PEG)
log (F_ν) [mJy]
log (ν) [Hz]
6
4
2
0
−2
−4
−6
8
10
12
14
16
18

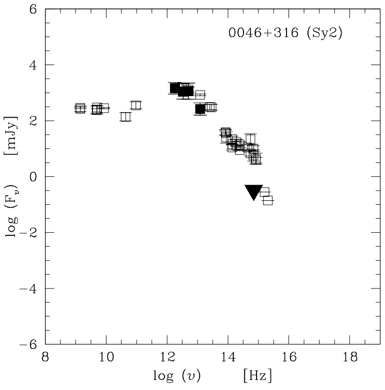
0046+316 (Sy2)
log (F_ν) [mJy]
log (ν) [Hz]
6
4
2
0
−2
−4
−6
8
10
12
14
16
18

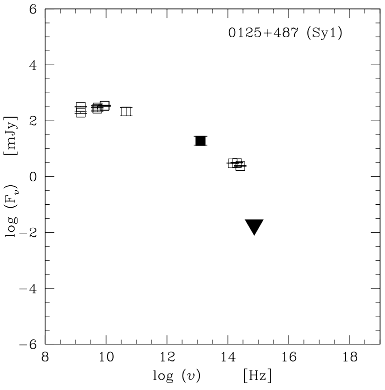
0125+487 (Sy1)
log (F_ν) [mJy]
log (ν) [Hz]
6
4
2
0
−2
−4
−6
8
10
12
14
16
18

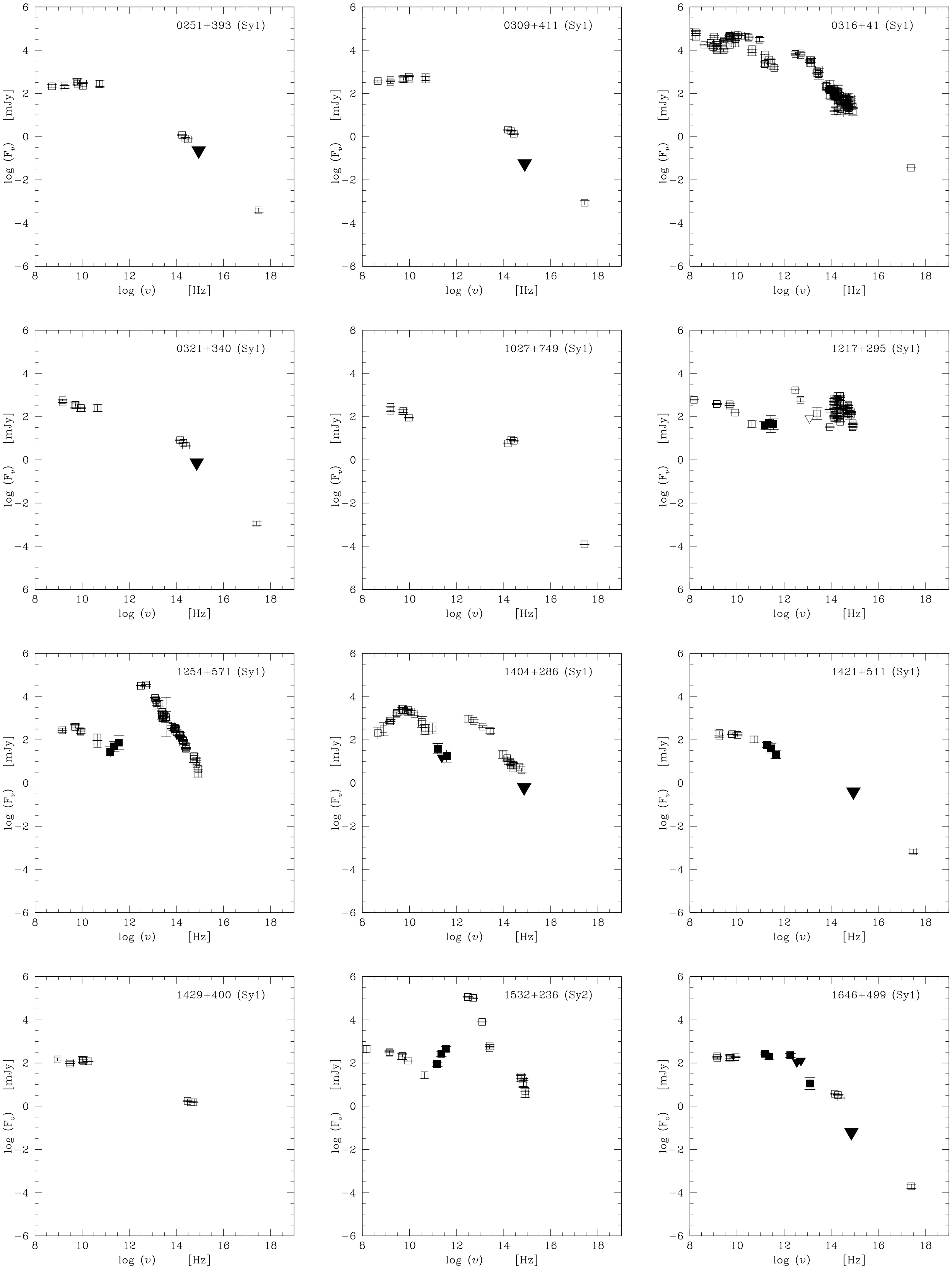
0251+393 (Sy1)
0309+411 (Sy1)
0316+41 (Sy1)
0321+340 (Sy1)
1027+749 (Sy1)
1217+295 (Sy1)
1254+571 (Sy1)
1404+286 (Sy1)
1421+511 (Sy1)
1429+400 (Sy1)
1532+236 (Sy2)
1646+499 (Sy1)
log (F$_\nu$) [mJy]
log (ν) [Hz]
6
4
2
0
−2
−4
−6
8
10
12
14
16
18

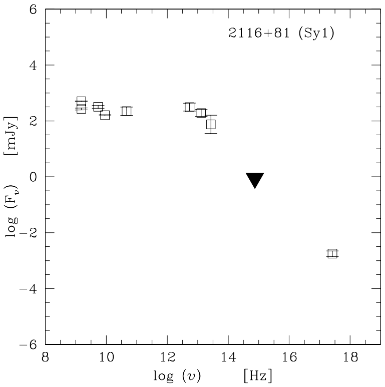
2116+81 (Sy1)
log (F$_\nu$) [mJy]
log (ν) [Hz]
6
4
2
0
−2
−4
−6
8
10
12
14
16
18

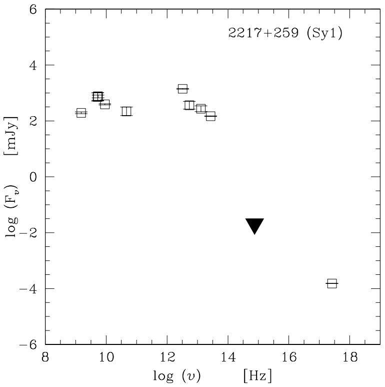
2217+259 (Sy1)
log (F$_\nu$) [mJy]
log (ν) [Hz]
6
4
2
0
−2
−4
−6
8
10
12
14
16
18

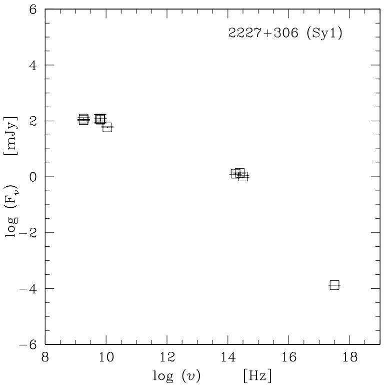
2227+306 (Sy1)
log (F$_\nu$) [mJy]
log (ν) [Hz]
6
4
2
0
−2
−4
−6
8
10
12
14
16
18

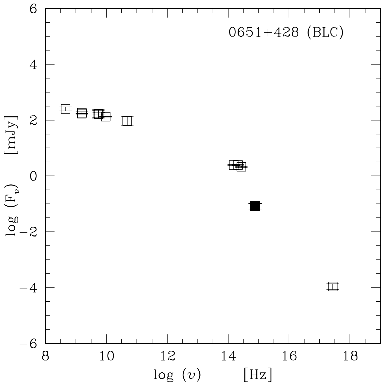
0651+428 (BLC)
log (F$_\nu$) [mJy]
log (ν) [Hz]
6
4
2
0
−2
−4
−6
8
10
12
14
16
18

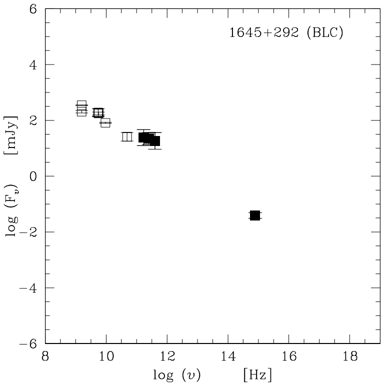
1645+292 (BLC)
log (F$_\nu$) [mJy]
log (ν) [Hz]
6
4
2
0
−2
−4
−6
8
10
12
14
16
18

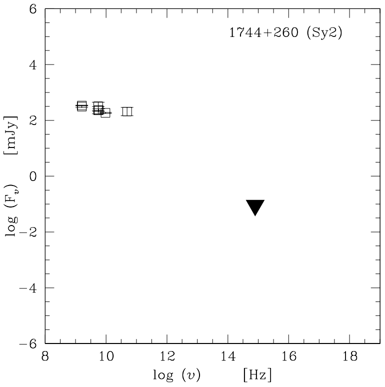
1744+260 (Sy2)
log (F$_\nu$) [mJy]
log (ν) [Hz]
6
4
2
0
−2
−4
−6
8
10
12
14
16
18

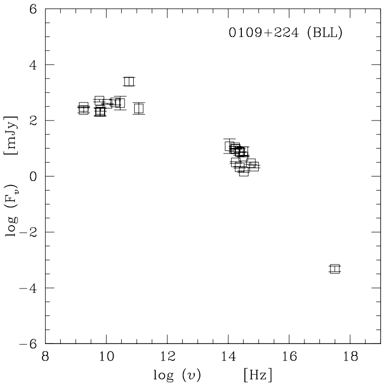
0109+224 (BLL)
log (F$_\nu$) [mJy]
log (ν) [Hz]
6
4
2
0
−2
−4
−6
8
10
12
14
16
18

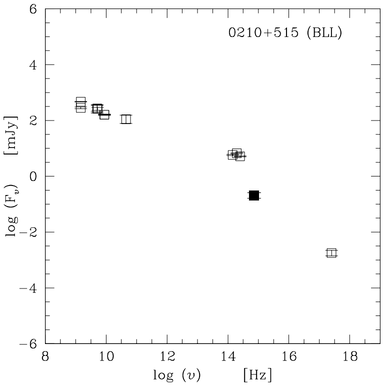
0210+515 (BLL)
log (F$_\nu$) [mJy]
log (ν) [Hz]
6
4
2
0
−2
−4
−6
8
10
12
14
16
18

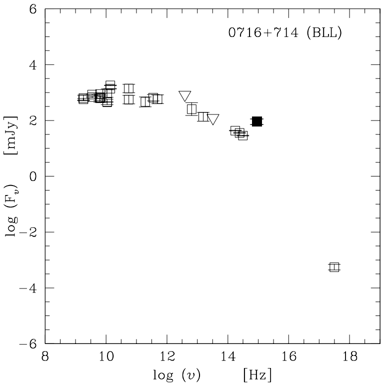
0716+714 (BLL)
log (F$_\nu$) [mJy]
log (ν) [Hz]
6
4
2
0
−2
−4
−6
8
10
12
14
16
18

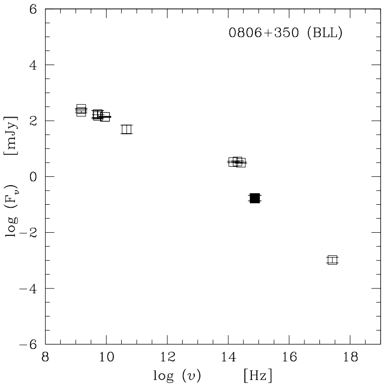
0806+350 (BLL)
log (F$_\nu$) [mJy]
log (ν) [Hz]
6
4
2
0
−2
−4
−6
8
10
12
14
16
18

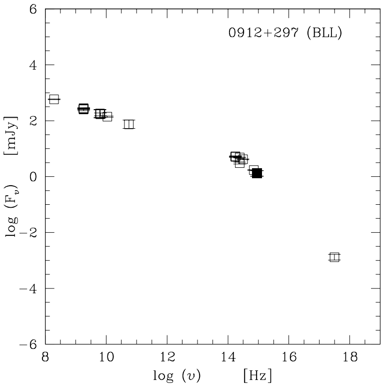
0912+297 (BLL)
log (F$_\nu$) [mJy]
log (ν) [Hz]
6
4
2
0
−2
−4
−6
8
10
12
14
16
18

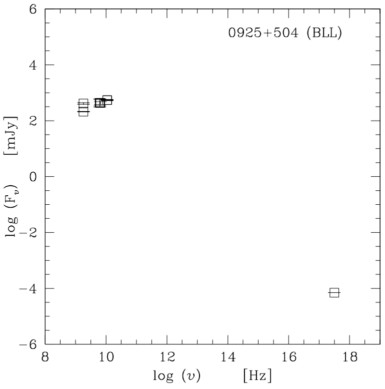
0925+504 (BLL)
log (F$_\nu$) [mJy]
log (ν) [Hz]
6
4
2
0
−2
−4
−6
8
10
12
14
16
18

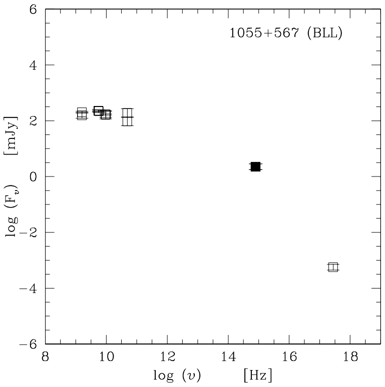
1055+567 (BLL)
log (F$_v$) [mJy]
log (v) [Hz]
6
4
2
0
−2
−4
−6
8
10
12
14
16
18

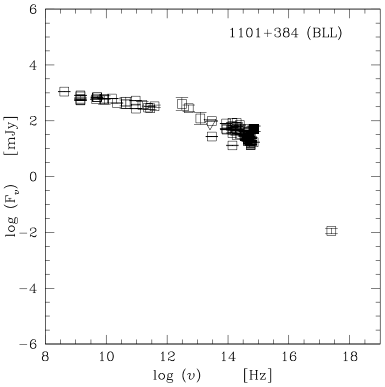
1101+384 (BLL)
log (F$_v$) [mJy]
log (v) [Hz]
6
4
2
0
−2
−4
−6
8
10
12
14
16
18

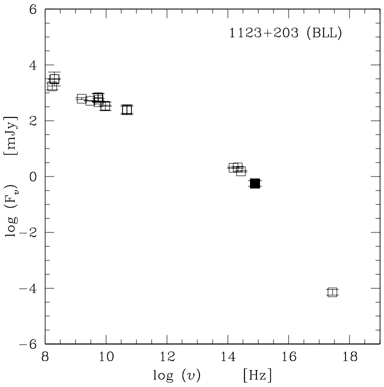
1123+203 (BLL)
log (F$_v$) [mJy]
log (v) [Hz]
6
4
2
0
−2
−4
−6
8
10
12
14
16
18

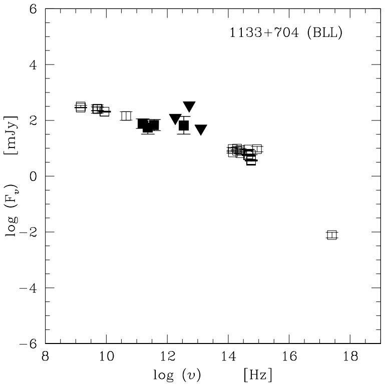
1133+704 (BLL)
log (F$_v$) [mJy]
log (v) [Hz]
6
4
2
0
−2
−4
−6
8
10
12
14
16
18

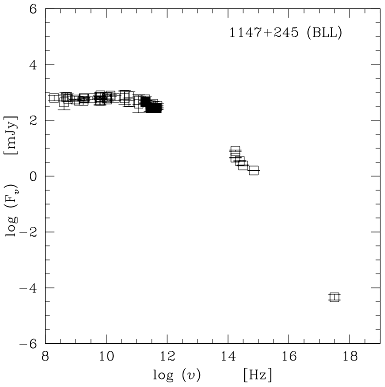
1147+245 (BLL)
log (F$_v$) [mJy]
log (v) [Hz]
6
4
2
0
−2
−4
−6
8
10
12
14
16
18

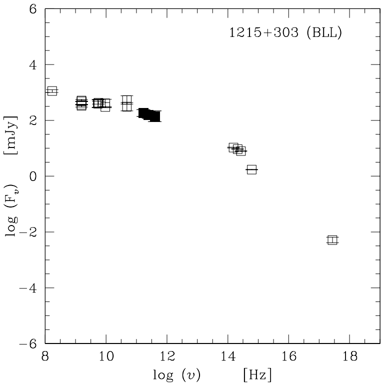
1215+303 (BLL)
log (F$_v$) [mJy]
log (v) [Hz]
6
4
2
0
−2
−4
−6
8
10
12
14
16
18

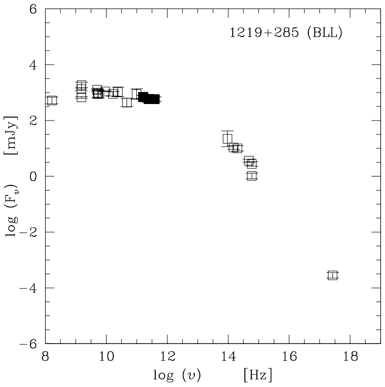
1219+285 (BLL)
log (F$_v$) [mJy]
log (v) [Hz]
6
4
2
0
−2
−4
−6
8
10
12
14
16
18

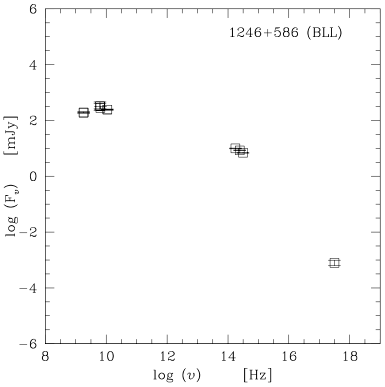
1246+586 (BLL)
log (F$_v$) [mJy]
log (v) [Hz]
6
4
2
0
−2
−4
−6
8
10
12
14
16
18

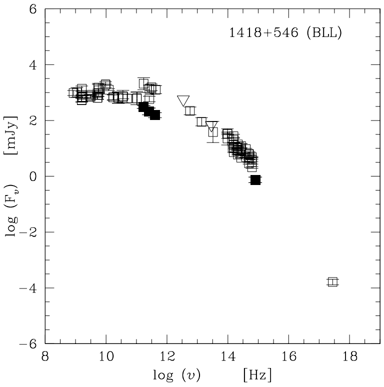
1418+546 (BLL)
log (F$_v$) [mJy]
log (v) [Hz]
6
4
2
0
−2
−4
−6
8
10
12
14
16
18

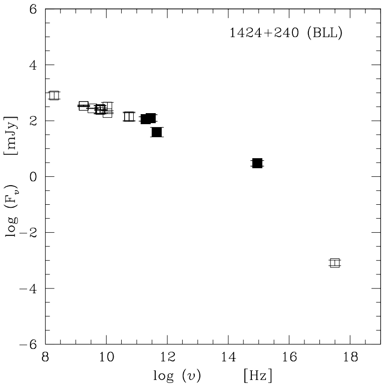
1424+240 (BLL)
log (F$_v$) [mJy]
log (v) [Hz]
6
4
2
0
−2
−4
−6
8
10
12
14
16
18

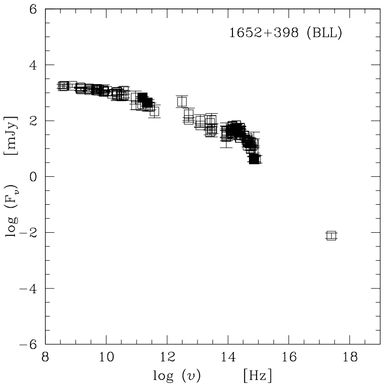
1652+398 (BLL)
log (F$_v$) [mJy]
log (v) [Hz]
6
4
2
0
−2
−4
−6
8
10
12
14
16
18

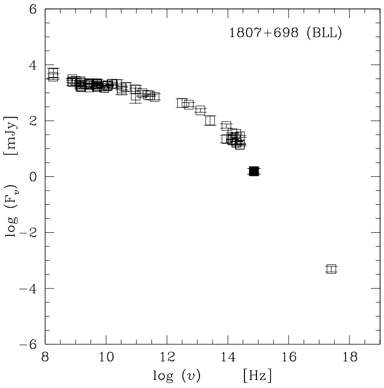
1807+698 (BLL)
log (F$_v$) [mJy]
log (v) [Hz]
6
4
2
0
−2
−4
−6
8
10
12
14
16
18

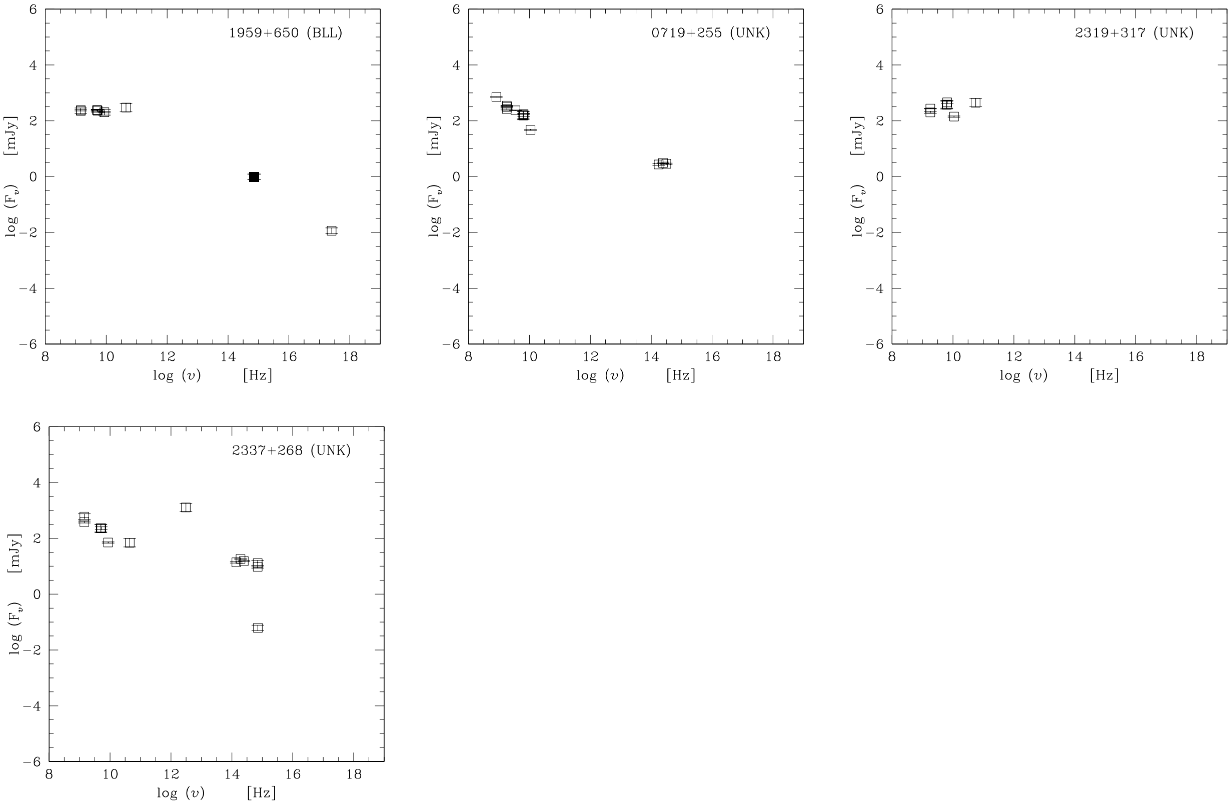

Figure A1. For each object the SED in units of log (F$_\nu$) *vs* log (ν). The objects are ordered by optical classification, the first group being the PEGs, then the Seyfert-like objects, then the BL Lac candidates, then the BL Lacs, and finally 3 objects for which are missing optical spectra and are marked as UNK. Empty symbols represent data found in the literature and in the NASA/IPAC Extragalactic Database (NED). 2MASS JHK photometry and detections in the Bright *ROSAT* All-Sky Survey are included. Filled symbols represent the following data: SCUBA data - 150, 222 and 353 GHz; ISOPHOT data – 170, 90, 60 and 25 μm and Optical data – optical flux densities estimated through the 4000Å break contrast, F^{AGN} (see text). Inverted triangles represent upper limits. Note that in the case of PEGs and Seyfert-like objects the estimated F^{AGN} represents an upper limit, for this reason the data points are plotted as inverted big triangles.